Bubble-Induced Water Hammer and Cavitation in Microchannel Flow Boiling

David W. Fogg
Creare Inc,
P.O. Box 71,
Hanover, NH 03755
e-mail: dwf@creare.com

Kenneth E. Goodson
Department of Mechanical Engineering,
Stanford University,
Building 530, Room 224,
Stanford, CA 94305

While microchannel flow boiling has received much research attention, past work has not considered the impact of acoustic waves generated by rapidly nucleating bubbles. The present work provides a theoretical framework for these pressure waves, which resembles classical "water hammer" theory and predicts a strong influence on bubble nucleation rates and effective convection coefficients. These pressure waves result directly from confinement in microchannel geometries, reflect from geometrical transitions, and superimpose to create large transients in the static liquid pressure. Feedback from the pressure waves inhibits bubble growth rates, reducing the effective heat transfer. Pressure depressions generated by the propagating pressure pulses can cause other bubbles to grow at lower than expected wall temperatures. The additional nucleation enhances heat transfer over short times but increased flow instability may inhibit heat transfer over longer periods. The limited quantitative measurements available in the literature indicate confined bubble growth rates in microchannels are significantly lower than those predicted by the classical Rayleigh–Plesset equation. The present model predicts confined bubble growth rates to within ± 20%. A nondimensional number indicative of the relative magnitude of the water hammer pressure to bubble pressure is proposed to characterize the transitions from conventional to microchannel flow boiling. [DOI: 10.1115/1.3216381]

Keywords: microchannel, flow boiling, confinement, two-phase heat transfer, bubble acoustics, water hammer

1 Introduction

The semiconductor industry continues to increase the total number, number density, and power density of transistors in microprocessors. The resulting trend in device design is leading to highly nonuniform heat generation and increasing power consumption by the chips [1]. In the near future, forced air convection will be replaced by liquid microchannel cooling technologies in an effort to drive the resistance of the chip package down and allow larger heat exchangers to be located remotely in the computer chassis. Two-phase microchannel cooling promises increased performance by further reducing the package resistance while still allowing a remote exchanger to reject the waste heat to the environment.

Notwithstanding the concentrated research effort in this field, fundamental challenges in controlling the pressure and temperature fluctuations remain, preventing accurate predictions of performance and reliability. Oscillations in temperature and pressure have been observed in both single channels [2] and multichannel arrays [3,4]. Qu and Mudawar [3] observed pressure drop and parallel channel instabilities in an array of 21 231×712 μm^2 rectangular channels. The pressure drop instability is a result of the flow rate response of the flow delivery system to pressure changes in the test section. Frequencies are usually very low on the order of 0.1 Hz. In the parallel channel instability, the flow redistributes itself in response to an increased pressure drop in a few channels due to nonuniform vapor generation. Peles [4] also observed parallel channel and pressure drop instabilities in 13 channel arrays of 50–200 μm triangular channels. A flow excursion instability resulting from flow regime transitions and a compound relaxation instability from rapid bubble growth were also observed. Peles [4] noted that the instabilities were more pronounced in the microchannels than they are for large channels. Zhang et al. [2] observed pressure oscillations and periodic vapor generation in single rectangular microchannels measuring 44 μm and 113 μm in hydraulic diameter under constant applied heat flux and constant inlet velocity boundary conditions. The resulting oscillations were classified a compound relaxation instability similar to bumping and geysering and was associated with the rapid vapor generation characteristic of microchannels. For detailed descriptions of two-phase flow instabilities refer to Boure et al. [5] or Carey [6].

Understanding the dynamic behavior of microchannel flow boiling is a major challenge, as the metrology and modeling for these flows are still in their infancy relative to larger scale systems. Due to the spatial constraints of the system, measurements have been limited to inlet and outlet pressures from commercial pressure taps, flow rates with commercial flow meters, wall temperatures with IR thermometry or microfabricated thermistors, and high speed video imaging [2,3,7–10]. The inability to directly measure flow parameters in the channel itself leads to a great deal of uncertainty as it forces assumptions to be made in order to interpolate local values from those measured externally. Research is ongoing to identify techniques to measure parameters such as void fraction [11,12] and local liquid temperature [12] but further work is required before they can be applied to obtain reliable quantitative values.

Numerical and analytical studies can provide insight into these flows in the absence of direct experimental evidence. To date, the bulk of microchannel two-phase research has been experimental, but several analytical and numerical studies have been performed. Chavan et al. [13] analytically examined the stability of two-phase forced convection in microchannels using a homogeneous flow linear stability model. This model was previously applied to macroscale flows. The model predicts the pressure response for a single channel to perturbations in inlet velocity and Chavan concludes that microchannel forced convective boiling is only stable for low subcooling and low applied heat fluxes. Consequently,

Contributed by the Heat Transfer Division of ASME for publication in the JOURNAL OF HEAT TRANSFER. Manuscript received February 13, 2008; final manuscript received October 7, 2008; published online October 15, 2009.

these systems are inherently unstable at practical operating conditions. Zhang et al. [10] modeled a single channel using a steady-state one-dimensional homogeneous model in which conjugate wall conduction was considered. The model showed reasonable agreement with experimental single channel data. This model was later extended to estimate the thermal performance for 3D logic architectures [14]. Ajaev and Homsy [15] numerically investigated constrained vapor bubbles next to a heated wall. The simulations included 2D and 3D steady bubbles in which condensation at colder regions of the interface balanced the evaporation at the heated regions, as well as the growth of a 2D bubble under higher thermal loads. Mukherjee and Kandlikar [16] used a level set method to simulate the growth of constrained bubbles in a superheated liquid showing good agreement with experiments in interface growth rates and overall bubble shape. The model was later used to investigate the role of inlet constrictions on the ejection of vapor bubbles from microchannels [17].

One assumption common to all of these models is that the liquid is incompressible. They also neglect the bubble nucleation process assuming a bubble already exists. Homogeneous models do not consider individual bubbles but treat the two-phase mixture as a single pseudofluid. It has been speculated that the rapid growth of bubbles in microchannels generates pressure pulses within the channel [18], but little to no research, either experimental or analytical, has focused on this aspect of confined flow boiling. Rapid gas production during severe accidents in light water reactors are known to generate significant water hammer pulses in macroscale systems [19]. This analysis examines the role liquid compressibility plays in the nucleation, growth, and associated heat transfer of vapor bubbles in confined channels. The results indicate the heat and mass transfer during nucleate boiling in microchannels is inhibited by the confined geometry. Single bubbles can also trigger additional nucleation elsewhere in the channel leading to increased flow instability. This analysis identifies a nondimensional parameter to characterize the transition from conventional to microscale flow boiling.

2 Numerical Model

The following one-dimensional fully compressible Lagrangian–Eulerian finite-volume scheme is formulated to investigate the effect confined geometries have on microchannel flow boiling. The channels considered for the numerical model are square in cross section. The Rayleigh–Plesset model, described in detail later, is used to predict the growth of a spherical bubble. This growth model has been used extensively in other fields such as cavitation [20], sonoluminescence [21], and boiling [22]. The simulations are restricted to bubble diameters less than 50% of the channel diameter to avoid situations where the walls cause the bubbles to become nonspherical.

In this model, the liquid is captured with the Eulerian elements, while each bubble is tracked as a single Lagrangian structure. The Lagrangian–Eulerian approach allows a coarser discretization in the Eulerian grids thereby increasing the maximum allowable time step, while at the same time, retaining subelement resolution for the size and location of the bubbles. A fully discretized two- or three-dimensional compressible model requires extremely short time steps to avoid CFL instability issues.

2.1 Nucleation. For a two-phase microchannel heat exchanger to be effective for applications such as microprocessor cooling, boiling must occur well below the kinetic limit for homogeneous nucleation. In a practical heat exchanger, wall structures serve as heterogeneous nucleation sites. Nucleation starts because vapor embryos trapped in wall cavities are conducive to growth under the appropriate conditions. A nucleation site activates when the internal vapor pressure in a wall cavity exceeds the combination of surface tension and the external pressure,

$$P_b \geq P_l + \frac{2\sigma}{r_{\mathrm{ns}}} \tag{1}$$

The pressure inside the cavity is at the vapor pressure at the local wall temperature. The criterion can be rewritten as

$$T_w \geq T_{\mathrm{sat}}\left(P_l + \frac{2\sigma}{r_{\mathrm{ns}}}\right) \tag{2}$$

2.2 Bubble Initial Conditions. Initially, the interface is stationary,

$$\dot{r}_b = 0 \tag{3}$$

The nucleating bubble is treated as a sphere throughout the simulated growth and the initial volume is

$$V_b = \frac{4}{3}\pi r_{\mathrm{ns}}^3 \tag{4}$$

The bubble temperature is the local wall temperature, $T_b = T_w$, while pressure is the saturation pressure at the bubble temperature, $P_b = P_{sat}(T_b)$, and mass is obtained from the ideal gas law:

$$m_b = \frac{P_b V_b}{R T_b} \tag{5}$$

2.3 Heat and Mass Transfer. After a bubble has nucleated, heat and mass transfer between the liquid and the vapor are monitored. During the early inertia-controlled stage of growth, the vapor inside the bubble remains isothermal due to the thin thermal boundary layer surrounding the bubble. The bubble pressure remains constant for an isothermal bubble. As the bubble grows into the thermally controlled regime, transport of energy across the thermal boundary layer surrounding the bubble eventually limits the evaporation process.

To accurately capture the heat and mass transfer into a bubble growing in a microchannel, the full three-dimensional thermal convection problem should be solved, but this is computationally expensive and time consuming. In this study, the heat transfer rate is calculated as

$$\dot{q}_{\mathrm{lv}} = A_{b,s} h_{\mathrm{tp}} (T_w - T_b) \tag{6}$$

The two-phase heat transfer coefficient, h_{tp}, can be determined from a microchannel heat transfer correlation [23,24] or taken as a fixed effective value.

Considering the correlations are not derived for single bubble physics, the heat transfer coefficient in this study is a constant. Significant insight into the expected behavior can be obtained with this one-dimensional model by examining reasonable limits to the thermal transport. Infinite heat transfer, corresponding to an isothermal bubble at the nucleation temperature, provides the upper limit to the heat transfer into the bubble, while an effective two-phase heat transfer coefficient on the order of the single-phase convective coefficient serves as the lower limit. The heat transfer coefficient for a single bubble should be greater than the spatially averaged heat transfer coefficient typically reported for flow boiling in a microchannel. Except for the section where the effect of the heat transfer coefficient is evaluated, the analysis presented in this article assumes infinite heat transfer corresponding to inertia-controlled growth.

Mass transfer into the bubble is calculated directly from the heat transfer to the bubble and an enthalpy balance. The model accounts for the sensible heat required to raise the vaporized liquid to the bubble temperature, any temperature changes to the previous mass in the bubble, and the latent heat of vaporization, i_{lv}.

$$\frac{dm_b}{dt} = \frac{\dot{q}_{\mathrm{lv}} - m_b C p_v \dfrac{dT_b}{dt}}{C p_l (T_b - T_l) + i_{\mathrm{lv}}} \tag{7}$$

The saturated vapor inside the bubble is modeled as an ideal gas. Changes in pressure with respect to temperature are given by the Clausius–Clapeyron equation [25].

$$\left(\frac{dP_b}{dT_b}\right)_{\text{sat}} = \frac{i_{\text{lv}}}{T_b(v_v - v_l)} \tag{8}$$

Differentiating the ideal gas law and substituting Eq. (8) provides the expression for the change in temperature with respect to specific volume

$$\left(\frac{dT_b}{dv_v}\right)_{\text{sat}} = \frac{P_b}{R - \dfrac{v_v i_{\text{lv}}}{T_b(v_v - v_l)}} \tag{9}$$

The bubble pressure is the saturation pressure at the bubble temperature. For many fluids including water, the saturation pressure is well correlated with the saturation temperature using a form derived from the Clapeyron equation [25].

$$\ln P_{\text{sat}} = \frac{T_c \ln P_c}{T_c - T_{\text{boil}}}\left(1 - \frac{T_{\text{boil}}}{T_b}\right) \tag{10}$$

where pressures are in bars and temperatures are in Kelvin.

2.4 Interface Velocity. The Rayleigh–Plesset equation models the growth or collapse of a spherical bubble from an active nucleation site in an infinite incompressible fluid [20].

$$\frac{P_b(t) - P_l(t)}{\rho_f} = r_b\ddot{r}_b + \frac{3}{2}(\dot{r}_b)^2 + \frac{4\eta_l\dot{r}_b}{r_b} + \frac{2\sigma}{\rho_l r_b} \tag{11}$$

The driving pressure gradient, $P_b - P_l - 2\sigma/r_b$, between the vapor and liquid can vary in time. In order to remain consistent with the geometry for which Rayleigh–Plesset equation was derived, the bubble is assumed to grow as a sphere. Consequently, the results presented correspond to early bubble growth where the shapes of bubbles in square channels have yet to be influenced by the walls. The accuracy of the Rayleigh–Plesset model should be questioned for bubbles that have grown to the size of the channel. As the interface approaches a wall, the interface velocity would be better approximated by a lubrication theory approach.

2.5 Liquid. The liquid is captured using staggered Eulerian grids consisting of the channel with the bubble volumes subtracted from each cell in which a bubble or part of a bubble exists. The linearized equation of state (Eq. (15)) accounts for the compressibility of the liquid, and changes in volume are captured through the use of the local void fraction, α. The grids are one-dimensional with cell divisions in the streamwise direction. Each element is uniform in length but can have different transverse dimensions allowing for varying channel cross sections. The staggered grid avoids the odd-even numerical instability arising from pressure-velocity coupling in centrally differenced convection terms [26]. The pressure grid is used to calculate density, pressure, enthalpy, and temperature, while the velocity grid is used only for liquid velocity.

2.6 Equations. The numerical approach solves the one-dimensional Navier–Stokes equations along with the convective energy equation and an appropriate equation of state.

$$\frac{\partial(\rho_l\alpha)}{\partial t} + \frac{1}{A_{\text{ch}}}\frac{\partial}{\partial z}(\rho_l U_l \alpha A_{\text{ch}}) = \sum_{k=1}^{nb}\frac{d\rho_{v,k}}{dt}\frac{A_{b,k}}{A_{\text{ch}}} \tag{12}$$

$$\frac{\partial}{\partial t}(\rho_l U_l \alpha) + \frac{1}{A_{\text{ch}}}\frac{\partial}{\partial z}(\rho_l U_l^2 \alpha A_{\text{ch}}) = -\frac{\partial P_l}{\partial z} + \frac{1}{A_{\text{ch}}}\frac{\partial}{\partial z}\sum \mathcal{F} \tag{13}$$

$$\frac{\partial}{\partial t}(\rho_l i_l \alpha) + \frac{1}{A_{\text{ch}}}\frac{\partial}{\partial z}(\rho_l U_l i_l \alpha A_{\text{ch}}) = \frac{1}{A_{\text{ch}}}\left(P_h h_{\text{tp}}(T_w - T_l) - \frac{\partial \dot{q}_{\text{lv}}}{\partial z}\right) \tag{14}$$

$$P_l = P_{l,0} + a_l^2(\rho_l - \rho_{l,0}) \tag{15}$$

These equations account for mass transfer between the phases and any forces, $\mathcal{F}$, including viscous shear, imposed on the liquid by the liquid-vapor or liquid-wall interfaces. The equation of state is a linearization about a reference point of 1 atm at room temperature for a liquid speed of sound, a_l. The bubble interactions with the liquid grids change the cell volumes and flux areas through the local void fraction, α.

2.7 Solution Algorithm. The numerical model is solved with an iterative segregated system. Semi-implicit temporal discretization prevents large overshoots in pressure and void dependent quantities, such as two-phase frictional pressure drop and heat transfer coefficient, while centrally differenced spatial discretization allows propagation in both directions. A tridiagonal matrix algorithm (TDMA) [26] solves each matrix system.

For each time step, the wall temperature, liquid density, liquid velocity, and liquid enthalpy or temperature are solved in order in an iterative loop. The new wall temperatures and liquid pressures are used to determine if any new nucleation sites have become active. Any new bubbles are initialized and the evolution of existing bubbles is calculated. A time step is considered to converge when the difference norm of the residuals has fallen by at least three orders of magnitude and total mass and energy are conserved to within 0.1%.

A grid convergence study was performed to determine the influence discretization has on the prediction of bubble growth rates. Eulerian grids of 75, 150, and 300 elements were used to predict the growth of a bubble with a constant pressure of 1.8 bar in a 2 cm long channel. Little difference was observed between the grids with 150 and 300 elements. Grid densities of 150 elements/cm are used for the remaining simulations.

3 Results and Discussion

3.1 Initial Bubble Growth. For this discussion, *confinement* in any direction refers to an obstruction preventing the liquid from moving in a direction, while *constrained* indicates the bubble interface is pressed against the obstruction preventing further growth in that direction. A truly unconfined bubble only exists in theory as practical systems are enclosed by boundaries. However, many systems are large enough that bubble growth is well approximated by the theory for unconfined bubbles. This is not the case for microchannels.

Let's review unconfined inertia-controlled bubble growth before exploring bubbles in microchannels. An *unconfined* isothermal bubble grows according to the Rayleigh–Plesset equation (Eq. (11)). For isothermal or inertia-controlled bubble growth, the heat transfer is sufficient to maintain a constant bubble pressure. After an initial period of acceleration, the interface asymptotes to a constant velocity presuming $r_b \gg r_{b,0}$.

$$\dot{r}_b = \left[\frac{2(P_b - P_l)}{3\rho_l}\right]^{1/2} \tag{16}$$

In this situation, the volume of the spherical bubble increases as t^3 because the volume goes as r_b^3.

Now assume the bubble is constrained in one dimension, by a pair of parallel walls in a high-aspect ratio channel for example. Such a bubble takes on the shape of a squat cylinder or a pancake. The diameter is free to grow but the thickness is restricted by the spacing of the parallel walls. If there is adequate heat transfer to keep the bubble pressure constant, the free interface still asymptotes to a constant velocity. The free portion of the interface remains inertia-controlled even though part of the interface is constrained. Neglecting wall friction this velocity is given by Eq. (16). In this case the volume grows with t^2 since the bubble is constrained by the spacing of the parallel walls. Following this rationale, the volume of an inertia-controlled bubble constrained in two dimensions, say by the four walls of a long rectangular

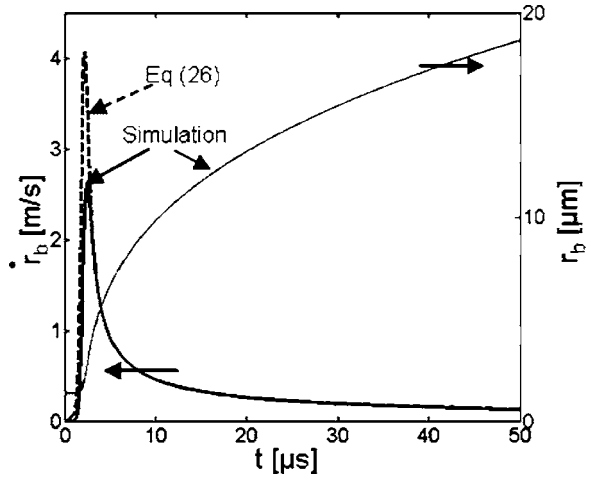

Fig. 1 Growth history for a bubble nucleating from a cavity (d_{ns}=2.75 μm, $T_b - T_w$=20 K) in a 100 μm square microchannel

channel, increases linearly with time. As discussed later, experiments by Fogg and Goodson [27] demonstrated that these trends do not hold for confined boiling in microchannels.

The radial growth for a confined bubble nucleating from a 2.75 μm diameter cavity in a 100 μm square channel is depicted in Fig. 1. Inertia-controlled growth is dominated by the liquid inertia. During this stage, heat and mass transfer are sufficient to maintain the bubble pressure at its initial value. After an acceleration period the interface velocity asymptotes to the value given by Eq. (16).

At some point, the channel confinement significantly affects growth. For water the specific volume of the liquid phase is three orders of magnitude smaller than the vapor phase. As a bubble grows, the liquid pressure increases to accommodate the rapidly displaced volume of liquid. The capacity of the channel to deal with this liquid diminishes with decreasing cross-sectional area. The increase in pressure propagates axially through the channel both upstream and downstream.

The resulting *confinement pressure*, P_{con}, comes from the rapid reduction in volume available for the liquid to occupy. It arises in the numerical model from terms involving $d(\rho\alpha)/dt$. Note that P_{con} is not influenced by the water bulk velocity. The additional term corresponding to the P_{con} superimposes onto the frictional and accelerational contributions to the pressure profile.

One can derive a simple expression for P_{con}, by considering a control mass of liquid surrounding a growing bubble, which is compressing the liquid. Symmetry allows the analysis to consider only $\frac{1}{2}$ of the bubble. The control mass should be sized, $dx=a_l dt$, such that any change in pressure due to the expanding bubble propagates right to the edge of the control mass. Since P_{con} depends on the change in volume, smearing the bubble into a rectangular volume, which spans the channel cross section, simplifies the analysis without changing the results for this one-dimensional derivation.

The choice of the control mass ensures that

$$V_l d\rho_l = -\rho_l dV_l \tag{17}$$

An increase in the volumetric growth rate of the bubble causes the volume of the control mass to shrink at $\frac{1}{2}$ the rate of the bubble growth.

$$\frac{d\dot{V}_b}{2} = -d\dot{V}_l \tag{18}$$

Although liquids are highly incompressible, they still are slightly compressible. The change in liquid pressure with respect to a change in density is

$$\frac{dP}{d\rho_l} = a_l^2 \tag{19}$$

After combining Eqs. (17)–(19) and recalling that $dx=a_l dt$, the change in pressure due to confinement, dP_{con}, is

$$dP_{con} = \frac{\rho_l a_l d\dot{V}_b}{2A_{ch}} \tag{20}$$

By integrating Eq. (20) from the initial condition of ($P_{con}=0$ and $\dot{V}_b=0$), the confinement pressure as a function of bubble volumetric growth rate is obtained.

$$P_{con} = \frac{\rho_l a_l \dot{V}_b}{2A_{ch}} \tag{21}$$

This derivation is remarkably similar to a piston compressing liquid in a one-dimensional duct [28]. The piston velocity corresponds to

$$\overline{\dot{r}_b} = \frac{\dot{V}_b}{2A_{ch}} \tag{22}$$

and P_{con} can be rewritten as

$$P_{con} = \rho_l \overline{\dot{r}_b} a_l \tag{23}$$

This pressure is the same form as the Joukowsky pressure [29] from water hammer theory. Thus, a bubble growing rapidly in a microchannel is comparable to a fast closing valve in a pipe, except the induced water hammer pressure influences bubble expansion. Increasing thermal loads and decreasing channel cross section exacerbate these water hammer effects. Although Eq. (23) provides the instantaneous liquid pressure, the maximum liquid pressure is estimated from the bubble pressure using the equality in Eq. (1). The confinement pressure can also be thought of as a bubble-generated acoustic pulse. Equation (22) corresponds to the particle velocity in one-dimensional acoustics and Eq. (23) is the sound pressure. The specific acoustic impedance is $P_{con}/\dot{r}_b=\rho_l a_l$.

One should note that the derivation above does not assume a particular growth behavior for the bubble. Since the confinement pressure depends on the volumetric growth rate, Eq. (21) can be applied to either inertia- or thermal-controlled growth. Of the two regimes, inertia-controlled growth will yield the higher confinement pressures for a given wall superheat.

If the water hammer or acoustic pulse reflections are neglected, confined bubble growth reaches a steady state when the effective bubble driving pressure balances the confinement pressure.

$$P_b - P_{f,0} - \frac{2\sigma}{r_b} = \frac{\rho_f a_f \dot{V}_b}{2A_{ch}} \tag{24}$$

When the interface is not constrained, the bubble remains spherical and the volumetric growth rate is

$$\dot{V}_b = 4\pi r_b^2 \dot{r}_b \tag{25}$$

Substituting Eq. (25) into Eq. (24) and specifying $P_b - P_{l,0} = 2\sigma/r_{ns}$ yields the radial growth rate as a function of bubble radius,

$$\dot{r}_b = \frac{\sigma A_{ch}(1 - r_{ns}/r_b)}{\pi\rho_l a_l r_{ns} r_b^2} \tag{26}$$

As shown in Fig. 1, Eq. (26) agrees with the numerical solution once the liquid pressure reaches steady state.

For a high-aspect ratio channel, the walls quickly constrain the

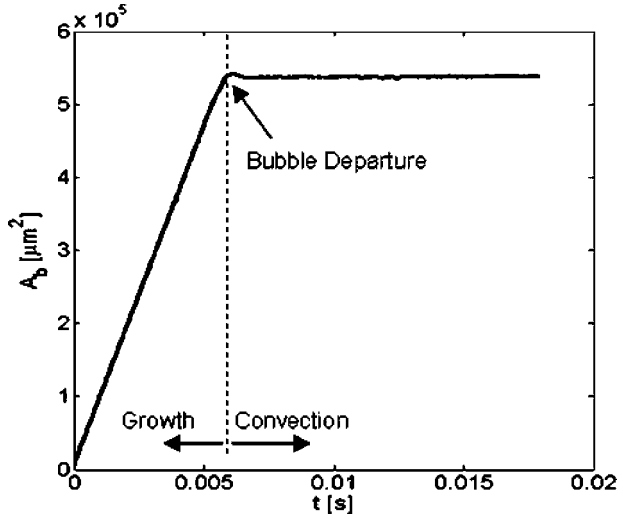

Fig. 2 Measured visible area of a pancake-shaped bubble growing in a 1000 μm by a 25 μm channel. Note the area grows linearly for this confined bubble and constrained in one dimension.

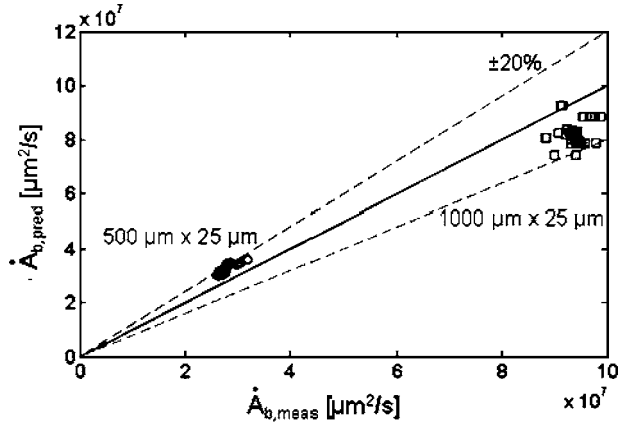

Fig. 3 Bubble growth rates measured in Ref. [29] are predicted within ±20% by the confinement pressure model

interface in one direction. In this case, the interface curvature is fixed by the critical channel dimension and the volumetric growth is, approximately,

$$\dot{V} = 2\pi r_b \dot{r}_b H_{\text{ch}} \tag{27}$$

The resulting radial growth rate in the unconstrained dimensions is

$$\dot{r}_b = \frac{2\sigma W_{\text{ch}}(1 - 2r_{\text{ns}}/H_{\text{ch}})}{\pi \rho_l a_l r_{\text{ns}} r_b} \tag{28}$$

Note the volumetric growth rate is constant because the effective driving pressure no longer varies with bubble radius.

Data collected by Fogg and Goodson [27] support this result. In the experiment, single inertia-controlled bubbles are simulated by injecting air through a 10–15 μm orifice in the center of high-aspect microchannels (1000×25 μm^2 and 500×25 μm^2). The supply air pressure, liquid flow rate, and liquid pressure drop are recorded by a data acquisition system, while a high-speed camera captures the bubble growth at 5000 fps. The measured evolution of the unconstrained cross-sectional bubble area is shown in Fig. 2. Unlike an unconfined bubble, constrained between infinite parallel plates, the pancake-shaped bubbles do not grow volumetrically as t^2 but rather linearly with time as predicted by Eqs. (27) and (28). As shown in Fig. 3, the model estimates the growth rates well. The ability to predict not only the temporal trend but also the growth rate indicates the model captures the key physics of confined bubble growth. Lee et al. [30] also measured constant volumetric growth rates for thermally grown pancake bubbles. This trend agrees with that predicted by the model, but may be associated with the temporal variation in the bubble pressure, which is not directly measured.

Reducing the channel cross-sectional area affects bubble growth as shown in Fig. 4. In all cases, initial growth is dominated by liquid inertia and channel confinement is negligible. Eventually the bubble grows large enough such that confinement pressure becomes significant relative to the bubble pressure, thereby retarding growth. The radius at which the confinement effect becomes noticeable scales with channel cross section. None of the bubble interface velocities in Fig. 4 reach the Rayleigh–Plesset asymptotic velocity (Eq. (16)) because feedback from the confinement pressure retards the volumetric growth. For a given wall superheat, the volumetric growth rate of bubbles in smaller channels is lower than that of bubbles in larger channels since the confinement pressure feedback occurs earlier in the growth process.

This result is particularly interesting since bubble growth in microchannels is often characterized as "explosive" [31] or "rapid" [32], yet this analysis predicts that microchannel bubble growth only appears rapid because of the relative scale of the channels to the bubbles. As shown in Table 1, the few measurements of interface velocities reported in the literature are lower than the Rayleigh–Plesset equation predictions for unconfined inertia-controlled growth at equivalent heating conditions. Although these studies seem to support the confinement pressure theory, they were not designed to capture the parametric dependence pertaining to growth velocities in microchannels. Based on the measurements reported, one is unable to determine whether the bubbles experience inertia- or thermal-controlled growth. The limited observations are insufficient to draw reliable conclusions.

Figure 5 illustrates the wall superheat effect on bubble growth. The pressure difference driving interface motion increases with temperature and leads to faster bubble growth. Surface tension is responsible for the time lag from the initiation of growth to the rapid acceleration of the interface. At the higher wall superheats

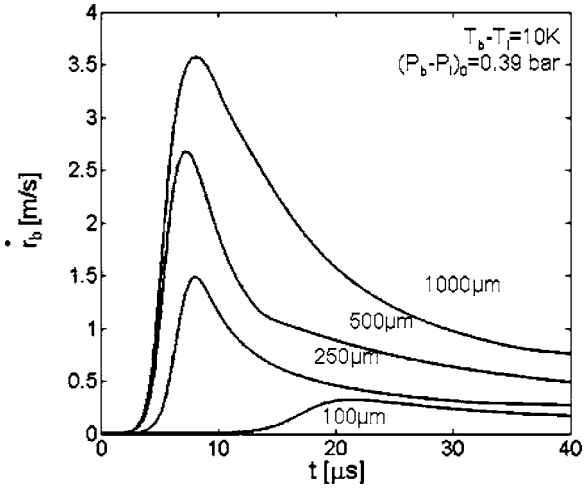

Fig. 4 The effect of reducing the channel cross-sectional area for bubbles nucleating at a wall superheat of 10 K, corresponding to a bubble overpressures of 0.39 bar. None of the bubble interfaces reach the asymptotic Rayleigh–Plesset velocity (Eq. (16)) before confinement retards growth.

Table 1 Comparison to interface velocities in the literature

Reference	Channel	Fluid	Max wall superheat (K)	Liquid pressure (kPa)	Max interface velocity (m/s)	Rayleigh–Plesset velocity (Eq. (16)) (m/s)
[31]	200–310 μm triangular	Water	6	101[a]	0.3	3.8
[40]	990×207 μm^2 rectangular	Water	9.5	101[a]	3.5	5.0
[41]	D_h=51.7 μm trapezoidal	Water	23	210	0.045	8.7

[a]Pressure not reported and assumed to be atmospheric.

the curvature of the bubble embryo is higher, and small increases in bubble radius rapidly reduce the opposing Laplace pressure, $2\sigma/r_b$. Higher superheats also lead to increased mass transfer.

One of the most significant unknowns in this model is the effective heat transfer coefficient. Existing experiments evaluate only average heat transfer. No microchannel studies for single bubbles have even been attempted. Lacking quality experimental data, models must assume a fixed value, as done in this study, or rely on heat transfer correlations [23,24] which are also time and spatially averaged.

Figure 6 shows how the heat transfer coefficient influences bubbles growing in water in a 100 μm square channel. The lowest value, 50 kW/m^2 approximates the value for single-phase liquid flow and serves as a lower limit. The upper limit corresponds to infinite heat transfer maintaining a constant bubble temperature and pressure. At lower heat transfer coefficients, bubble expansion reduces the bubble pressure and temperature due to insufficient phase change. However, heat transfer during inertia-controlled bubble growth is nearly infinite. After time, the superheat in thermal boundary layer becomes depleted and limits growth. From the analysis of Plesset and Zwick [22], this boundary layer grows roughly as the square root of time, $\delta_{th}\approx(\Lambda_l t)^{1/2}$ for a bubble in an otherwise quiescent infinite liquid at uniform superheat. For microchannels, the proximity of multiple walls enhances heat transfer. The Kandlikar correlation [33] predicts two-phase time-averaged microchannel heat transfer coefficients on the order of 100 kW/m^2 to 1 MW/m^2 for water depending on flow and heating conditions and channel geometry. The initial value for the heat transfer coefficient during bubble growth is much higher than the single-phase value and should be higher than the average heat transfer coefficients for microchannel flow boiling. Considering average h_{tp} is on the order of several hundred kW/m^2, the assumption of inertia-controlled growth for a small bubble appears reasonable. One should note that the confinement pressure depends on the volumetric growth rate of the bubble, whether or not bubble growth is inertia-controlled or heat transfer-controlled. The choice of a particular heat transfer coefficient merely changes the amplitude and evolution of the bubble-induced pressure pulse.

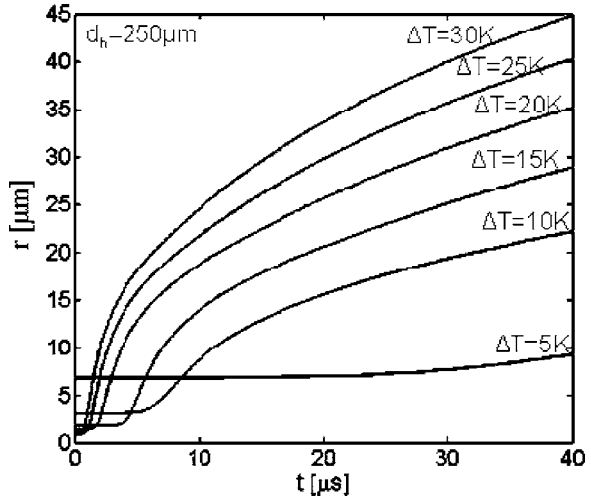

Fig. 5 The influence of wall superheat on a bubble growing in a square 250 μm channel

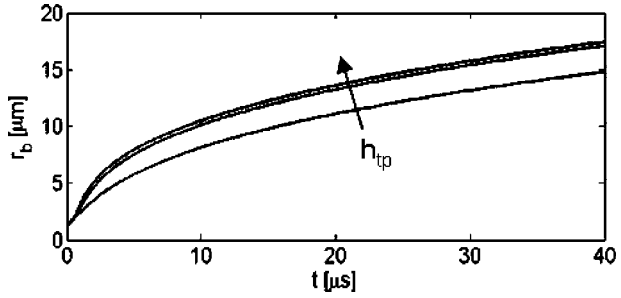

Fig. 6 The effect of heat transfer coefficient on bubble growth. The lines correspond to h_{tp}=50 kW/m^2, 500 kW/m^2, 5 MW/m^2, and 50 MW/m^2. The largest two lines are virtually on top of each other.

3.2 Heat Transfer. The majority heat transferred in flow boiling is due to phase change. The instantaneous heat transfer rate into the bubble is

$$\dot{q}_b = \rho_v \dot{V}_b i_{lv} \tag{29}$$

For an isothermal bubble ρ_v remains constant and the heat transfer rate is directly proportional to bubble growth. As discussed in Sec. 3.1, the bubble volumetric growth rate in microchannels is reduced from that in large channels because the confinement pressure retards growth. Thus, two-phase heat transfer is reduced for nucleate boiling in microchannels.

3.3 Channel Systems. The confinement pressure propagates through channel systems as water hammer or acoustic pressures travel through piping and duct systems. The pulses propagate both upstream and downstream. Microchannel heat exchangers contain various components including manifolds and headers, reducing and expansion junctions, inlet and outlet ports, as well as the tubing connecting the heat exchangers to the pump, reservoirs, and condenser. The combination of these various geometries dictates pressure pulse propagation.

To demonstrate the role geometry plays in pulse propagation and the ultimate impact on microchannel flow boiling, two single channel chip designs with different manifolds are simulated. The simulation includes system components from the channel up to inlet and outlet tubing. Both manifold geometries, shown in Fig. 7, are from single microchannel experiments [2,34]. The primary difference between the two designs lies in the manifold-to-channel transition. In the first design, the manifold suddenly steps down to the channel size, while in the second, the manifold tapers to the channel dimensions. The channels are 100 μm square and 2 cm long. The straight rectangular manifolds measure 600 μm wide, 250 μm deep, and 1 cm long [2]. The rectangular portions of the tapered manifolds measure 1000 μm wide by 100 μm deep and 9 mm long. They taper to the channel width over 1 mm creating a manifold 1 cm in total length [34]. The dimensions of the other components are summarized in Table 2. De-ionized water flowing

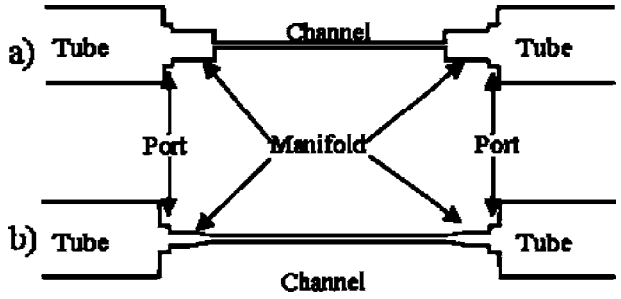

Fig. 7 Schematic of experimental manifold designs used in simulations to determine effect system design

at a Re=0.66 serves as the working fluid.

Figure 8 shows the pressure evolution inside the two channel systems for a bubble, located 1.45 cm ($z=0$) from the inlet manifold-channel junction, nucleating at a superheat of 20 K. This superheat corresponds to an initial pressure difference of $P_b - P_{l,0}=0.91$ bar. The bubble remains isothermal throughout its growth. At $t=3.5$ μs, the initial pulse reaches the transition to the outlet manifold. The reflected and transmitted portions of the pulse are seen propagating shortly thereafter. For the straight manifold, the portion of the pulse transmitted to the manifold is 12.5% of the pulse magnitude. The tapered manifold transmits 18.4% due to the more gradual area reduction. The reflections are inverted due to the expansion, locally reducing the liquid pressure. The pressure remains positive because they are superimposed on the incoming portion of the initial pulse.

At 10.5 μs, the upstream side of the initial pulse reaches the inlet manifolds. The reflections off the outlet manifolds have reached the bubble. An isothermal bubble approximates a constant pressure boundary leading to full reflections of incoming pulses.

By 16 μs, the initial pulse has reflected off the inlet manifold. The ratios of the reflected and transmitted pulses for each manifold design are the same as that for those at the outlet manifolds. The downstream pulse has also reflected off the manifold-port junction. Note that the pulse amplitudes transmitted into the tubing are negligible due to the large expansion between the ports and the tubing.

Direct experimental evidence of water hammer propagation in microchannel systems is difficult to obtain due to the spatial constraints imposed by the channels. The common measurement of inlet and outlet pressure in the tubing connected to the manifolds is incapable of capturing these pressure fluctuations due to the large expansions reflecting the pulses back into the system. The large cross-sectional area of the tubing readily absorbs any transmitted portion greatly reducing the measurable amplitude. A high-speed pressure sensor located in the microchannel itself needs to be developed to directly measure the water hammer pulses.

At 27 μs, multiple reflections have superimposed near the channel inlet to create a depression in the local liquid pressure below the operating pressure. As the bubble grows, the liquid pressure profile evolves ($t=44$ μs) with the confinement pressure propagation dictated by the channel system geometry. In the final set of profiles ($t=56$ μs), the multiple reflections superimpose creating a large pressure depression. In the straight manifold this depression is 10.0% of the bubble overpressure, $2\sigma/r_{ns}$, below the baseline pressure. For the tapered manifold, it is 14.4% below the baseline.

Figure 9 depicts the time history of the radial velocity and local liquid pressure for the bubble in the straight channel. After the initial acceleration, the bubble grows according to Eq. (26) until the first reflection off the manifold-channel junction returns to the bubble location. The bubble responds to the reduction in local liquid pressure by increasing its growth rate. This interface velocity remains at the increased level after the arrival of the manifold reflection because the bubble continues to emit a pressure front that negatively reflects back to the bubble location. Clearly, the channel system geometry significantly influences how the bubble-induced water hammer pressures propagate in microchannel systems influencing bubble growth, departure, convection, and nucleation. This feedback from the reflections of the bubble-induced water hammer indicates the channel system geometry can be engineered to manipulate the bubble growth and heat transfer rates.

3.4 Bubble Nucleation and Growth. The confinement pressure inhibits bubble growth but its subsequent propagation has the potential to promote additional nucleation. Water hammers are known to cause cavitation and water column separation [35]. Column separation in conventional channels usually occurs at one end of the water column when the liquid inertia essentially pulls the column away from a boundary creating a large void. Cavitation regions with low void fraction, known as dispersive column separation, are created by the propagation of a negative pulse slightly less than the local saturation pressure. Two negative pulses passing each other can lead to intermediate column separation as the superposition reduces the local pressure below the vapor pressure. Cavitation has been induced in small diameter channels with low-frequency ultrasound [36]. What remains to be answered is whether or not pressure depressions from water hammer reflections in microchannels can initiate and sustain boiling at normally inactive nucleation sites.

Figure 10 compares the local liquid pressure at $z=-11.4$ mm for the two channel systems in Sec. 3.3. In general, the evolution of the pressure is similar in both channels since the lengths and cross sections are comparable, but the taper does vary the reflections from the channel-manifold junction slightly. In the end, the tapered manifold leads to deeper troughs and higher peaks in the pressure for the situation simulated. The peaks in the liquid pressure can deactivate nucleation sites by forcing liquid into the cavities and flooding them. The troughs, on the other hand, have the potential to lead to additional nucleation.

As discussed before, a nucleation site will become active when the vapor pressure in a cavity exceeds the combination of surface tension and external pressure. Consequently, the pressure troughs should be capable of triggering bubble nucleation within the channel. Figure 11 displays the axial pressure distribution after the deepest trough has passed $z=-11.4$ mm in the tapered manifold design. As the trough passes ($t=56$ μs), a bubble nucleates from a 2.44 μm diameter cavity prescribed at $z=-11.4$ mm. The pressure increase due to the second bubble emerges in the confined channel. At $t=63$ μs, two pressure reflections are superimposed between the two bubbles to create a large pressure increase. A short while later, these pressure waves reflect off the bubbles creating another pressure trough, although this one is above the op-

Table 2 Dimensions of the microchannel systems depicted in Fig. 7. All lengths are in mm.

	Tubing			Port			Manifold			Taper				Channel		
System	W	H	L	W	H	L	W	H	L	W_1	W_2	H	L	W	H	L
A	2.8	2.8	20	1	1	0.5	0.6	0.25	10			NA		0.10	0.10	20
B	2.8	2.8	20	1	1	0.5	1	0.10	9	1	0.10	0.10	1	0.10	0.10	20

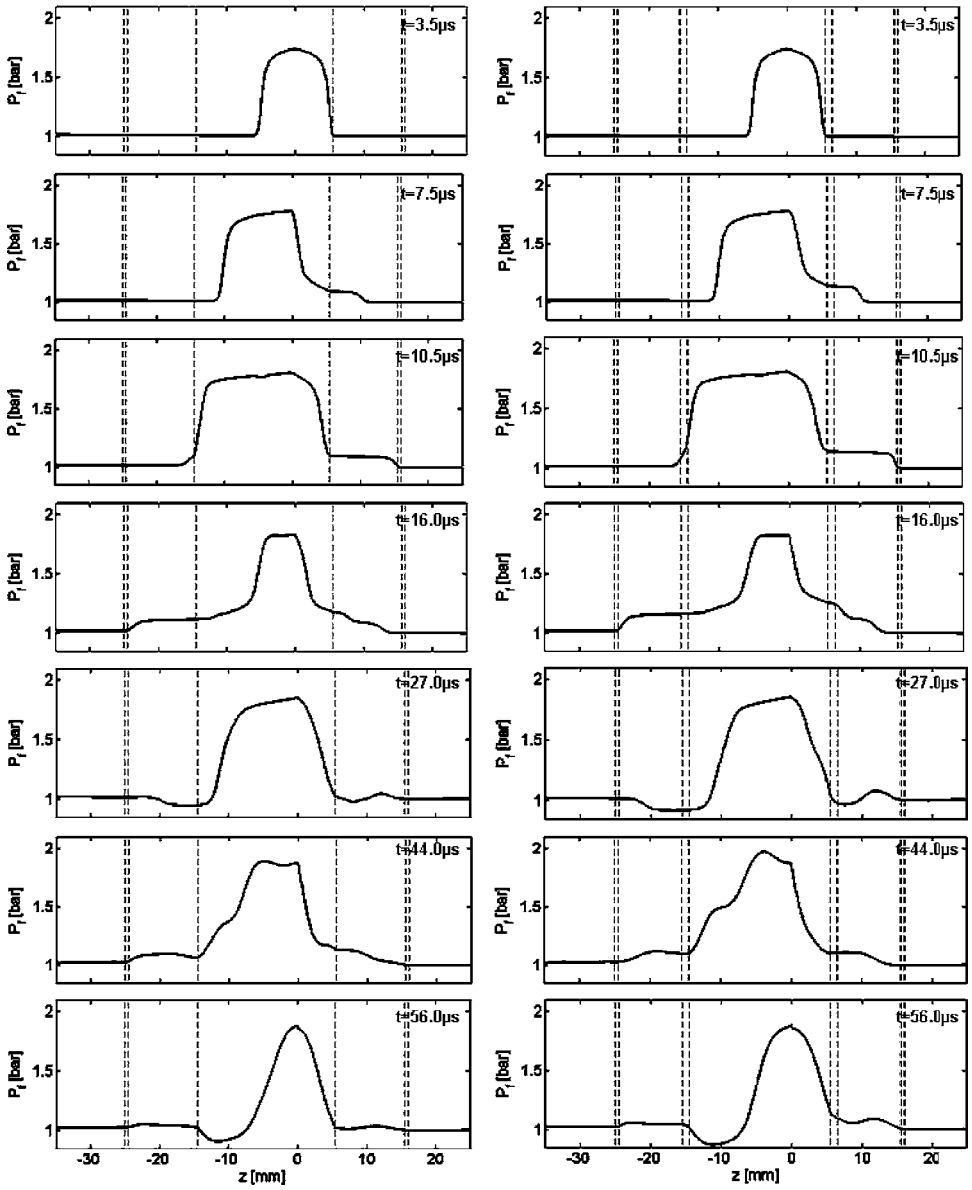

Fig. 8 Evolution of liquid pressure pulses in microchannel systems caused by the nucleation and growth of a single bubble. Straight manifold design (left) and tapered manifold design (right). The bubble nucleates at at $z=0$ for a wall superheat of 20 K and experiences inertia-controlled growth at a constant pressure throughout the simulation. The dashed lines denote axial locations with changes in channel geometry.

erating pressure. Figure 12 compares the time evolution of the liquid pressure for the tapered system with and without secondary nucleation at a location ($z=-6$ mm) between the two possible nucleation sites. The second bubble causes the maximum pressure to increase because the confinement pressure of the second bubble is added to the existing pressure. The oscillation period decreases since the pulse propagation length is between the two bubbles (11.4 mm) instead of the first bubble and the inlet manifold (15 mm).

Since the propagation of the acoustic pressures is dictated by a linear differential equation, the contributions of several bubbles superimpose in a channel. As displayed in Fig. 13, the bubble-induced water hammer from the second bubble influences the growth of the first bubble. For this case, the interface velocity of the first bubble is slightly affected by the second bubble, but the net effect on the bubble radius is negligible.

Because of the transient nature of the liquid pressure, the size of the nucleation site determines whether or not net bubble growth is realized at the secondary nucleation site. For a local wall superheat of 20 K, Fig. 14 plots the resulting bubble growth for nucleation sites of diameter 2.392 μm, 2.415 μm, and 2.557 μm from which bubbles start to grow once the local liquid pressure drops below 0.868 bar, 0.878 bar, and 0.936 bar, respectively. The minimum activation diameter for these conditions with the liquid pressure history in Fig. 10 is 2.3886 μm. Less than 30 nm means the difference between a bubble that continues to grow and one that collapses. If the nucleation site diameter is fixed, this corresponds to only a few tenths of a Kelvin in wall temperature. Therefore, for most wall temperatures greater than the minimum activation temperature, secondary bubbles will nucleate, grow, and depart in microchannels.

The additional nucleation and bubble growth generated by bubble-induced water hammer could have profound impacts on device performance. Vapor generated at lower than expected wall

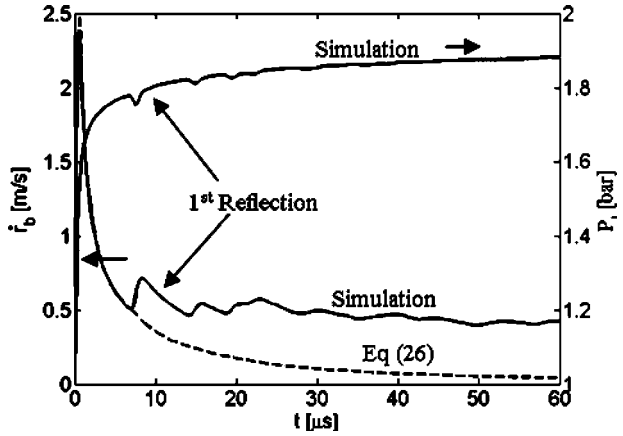

Fig. 9 Time history of the bubble radial velocity in the straight manifold channel. The negative water hammer reflections effectively increase the bubble growth rate.

temperatures improves heat transfer over short time periods. The thermal performance of similar channel geometries with different manifolds can vary significantly due to magnitudes of reflected water hammer pulses. Flow redistribution and associated instabilities will increase due to the increased channel pressure drop tied to the additional nucleation. In single microchannels, water hammer pulses can generate groups of bubbles at once similar to the compound relaxation instability observed by Zhang et al. [2]. The strong dependence on the overall system geometry makes it difficult to quantitatively compare results between different devices with the same channel dimensions.

3.5 Confinement Number. Microchannel flow boiling researchers have yet to identify a nondimensional parameter to describe the transition from conventional channels to microchannels. In the schemes proposed by Kandlikar and Grande [37] or Mehendale et al. [38], the size effect on flow boiling is characterized only by channel hydraulic diameter. For example, Kandlikar and Grande [37] classified flow boiling in channels as follows:

conventional channels: $d_h > 3$ mm
minichannels: 200 μm $< d_h \leq 3$ mm
microchannels: 10 μm $< d_h \leq 200$ μm
transition channels: 0.1 μm $< d_h \leq 10$ μm
molecular nanochannels: $d_h \leq 0.1$ μm

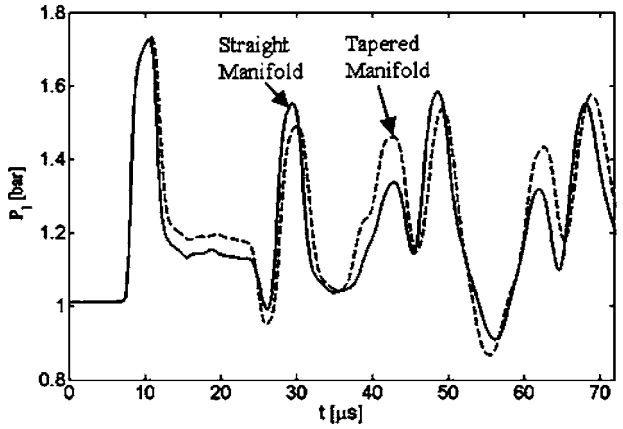

Fig. 10 Time evolution for the local liquid pressure at z= −11.4 mm. The bubbles nucleate at T_{sup}=20 K in both systems. The minimum P_l for the straight manifold is 0.909 bar and 0.866 bar for the tapered manifold.

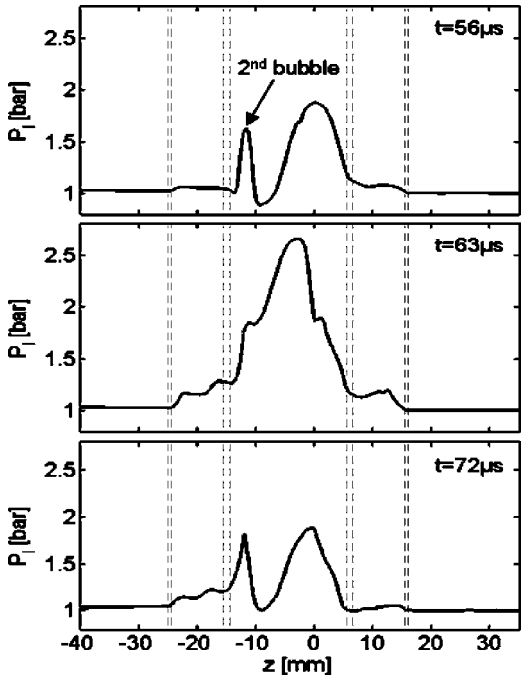

Fig. 11 The evolution of the static liquid pressure in the tapered channel if a 2.44 μm diameter cavity is located at z= −11.4 mm

Both classification schemes are based solely on qualitative experimental observations and do not necessarily reflect natural regime transitions due to fundamental physical phenomena.

A better system would predict phenomenological transitions using nondimensional numbers which may include the geometry, fluid properties, and other parameters indicative of shifts in the dominant physical mechanisms. Kew and Cornwell [39] recommended a confinement number,

$$\mathrm{Co}_{\mathrm{KC}} = \left[\frac{\sigma}{g(\rho_l - \rho_v)d_h^2}\right]^{1/2} \tag{30}$$

to differentiate between macroscale and microscale flow boiling. They found the flow characteristics and heat transfer were significantly different than macrochannel predictions when $\mathrm{Co}_{\mathrm{KC}} > 0.5$. For water at atmospheric pressure the transition based on this criterion is approximately 5 mm. The applicability of this number is questionable as scaling analysis typically indicates buoyancy is negligible for microchannels.

The increase in local liquid pressure is a fundamental confine-

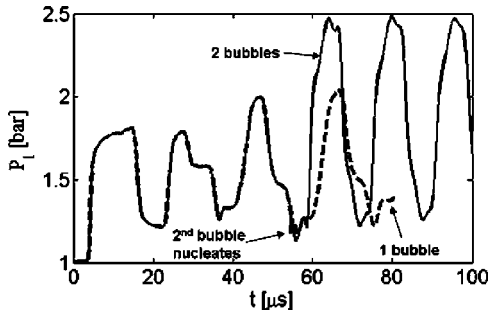

Fig. 12 Time history comparison of the liquid pressure at z= −6 mm for the tapered manifold channel with (solid line) and without (dashed line) additional nucleation from a 2.44 μm cavity at z=−11.4 mm

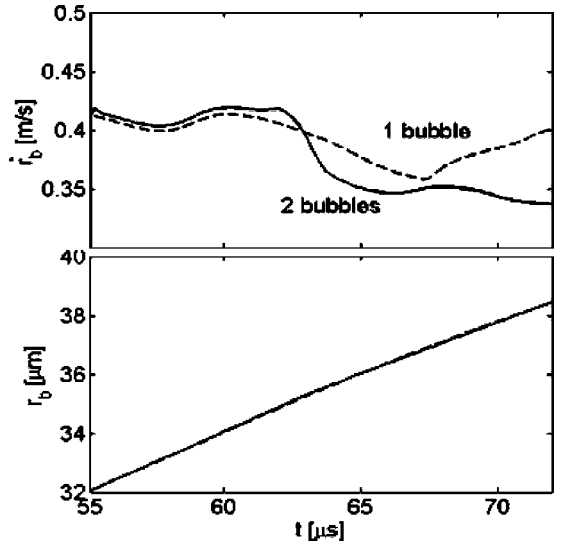

Fig. 13 Interaction of the second bubble in the tapered manifold channel with the growth of the first bubble

ment effect, presenting an opportunity to define a nondimensional number as the ratio of the confinement pressure to the bubble overpressure,

$$\mathrm{Co}_{\mathrm{FG}} \equiv \frac{P_{\mathrm{con}}}{P_b - P_{l,0}} \tag{31}$$

This number indicates magnitude of the feedback from the confinement pressure and can characterize the transition from conventional channels to microchannels. For channels large enough that the increases to the local liquid pressure are negligible, $P_{\mathrm{con}} \ll P_b - P_{l,0}$, $\mathrm{Co}_{\mathrm{FG}}$ is small. Large values for $\mathrm{Co}_{\mathrm{FG}}$ correspond to systems where the induced liquid pressure significantly inhibits volumetric growth.

Equation (31) can be applied to more than just single bubbles. The definition is rather general and can easily be applied to practical channel conditions at any instant in time. Since the confinement pressure is driven by the change in local liquid fraction, one could treat a pair of closely spaced bubbles that are about to coalesce as a single void. The volumetric growth rate of the combined void would then be used in Eq. (21). Furthermore, Eq. (31) could be applied to thermally controlled bubbles simply by using the saturation pressure, which corresponds to the instantaneous bubble temperature, for P_b. Only the parameter $P_{l,0}$ is fixed as it represents the liquid pressure the bubble would see if it is unconfined.

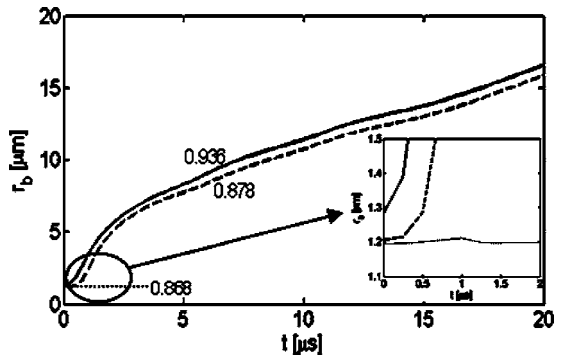

Fig. 14 The growth history for bubbles at $z=-11.4$ mm from sites nucleating at liquid pressures of 0.868 bar, 0.878 bar, and 0.936 bar for a $T_w=393.15$ K. These nucleation sites measure 2.392 μm, 2.415 μm and 2.557 μm in diameter, respectively.

For a certain set of assumptions, $\mathrm{Co}_{\mathrm{FG}}$ can be used to analytically estimate when a bubble becomes confined. Consider a relatively small inertia-controlled bubble that is not affected by channel confinement. The volumetric growth rate is determined by the interface velocity (Eq. (16)). The bubble overpressure can be approximated as $(P_b - P_{l,0}) = 2\sigma / r_{\mathrm{ns}}$. Substituting this relation and Eq. (21) into Eq. (31) allows the confinement number to be rewritten as

$$\mathrm{Co}_{\mathrm{FG}} = \frac{a_l \mathcal{G} r_b}{2A_{\mathrm{ch}}} \left(\frac{\rho_l r_{\mathrm{ns}}}{3\sigma} \right)^{0.5} \leq C_{\mathrm{con}} \tag{32}$$

The shape factor $\mathcal{G}$ accounts for the bubble geometry, which is introduced through the volumetric growth rate in Eq. (16). For a sphere $\mathcal{G} = 4\pi r_b$, while for a pancake-shaped bubble constrained in one dimension $\mathcal{G} = 2\pi H_{\mathrm{ch}}$. Equation (32) contains parameters representing the channel and bubble geometries as well as fluid properties. After specifying a confinement threshold, C_{con}, a confinement bubble diameter can be defined. For reference, the maximum radial velocity, noted in Fig. 1, for bubbles with superheats from 5 K to 30 K in channels (100 $\mu\mathrm{m} \leq d_h \leq 1$ mm) correspond to $0.11 < C_{\mathrm{con}} < 0.41$. The peak radial velocity occurs after P_{con} overcomes the driving pressure.

Ultimately, the threshold, C_{con}, at which channel confinement significantly influences bubble growth must be determined from experimental data. Such experiments need to measure both bubble growth and pressure over the growth cycle of single bubbles. A measurement of the bubble pressure is virtually impossible in heat transfer studies. With the exception of Ref. [29], the authors are unaware of any other study in the literature which monitors both these parameters for single bubbles in small channels. Furthermore, the range of channel diameters in Ref. [29] is insufficient to ascertain the confinement threshold. In lieu of an experimentally determined C_{con}, a logical choice is 0.1 indicating P_{con} is at least one order of magnitude less than the bubble driving pressure. This somewhat arbitrary value appears reasonable based on the simulation results. Eventually suitable experiments will need to be performed to properly characterize the true transition from an unconstrained bubble to a confined one.

Utilizing Eq. (27) one can define a critical nondimensional bubble cross section where the bubble begins to become confined. For a spherical bubble in a liquid, this is a function of the liquid properties and wall superheat.

$$A_b^* \equiv \frac{\pi r_b^2}{A_{\mathrm{ch}}} = \frac{C_{\mathrm{con}}}{2a_l} \left(\frac{3\sigma}{\rho_l r_{\mathrm{ns}}} \right)^{0.5} \tag{33}$$

The critical value increases with superheat because P_{con} based on the Rayleigh–Plesset asymptotic velocity (Eq. (16)) increases only with $P_b^{1/2}$. For a threshold value of $C_{\mathrm{con}}=0.1$, the nondimensional critical confinement bubble radius, $r_b^* = 2r_b/d_h$, for water in a square channel is approximately 2% of d_h. Hence, P_{con} becomes important for $r_b = 1$ μm, 10 μm, and 100 μm for $d_h = 100$ μm, 1 mm, and 1 cm, respectively. Assuming a bubble essentially stops growing once it departs from the wall, the effects of P_{con} are not realized for channels where the bubble departure diameter is less than the critical confinement diameter. These values qualitatively agree with experimental observations. For channels on the order of a few hundreds of micrometers, confinement is always observed. Millimeter-sized channels are reported to exhibit both conventional and microchannel behavior, while larger channels are well modeled by conventional theory. Note the above discussion assumes bubble pressure remains constant throughout the growth process. If bubble growth becomes thermally controlled, bubble growth slows, which would allow the bubble to become larger before the confinement pressure becomes significant.

4 Conclusions

Bubble-induced water hammers or acoustic pulses are one of the first confinement effects to be modeled. The additional acoustic pressure inherent to microchannel flow boiling plays an important role in the dynamic behavior of the flows. Depending on the level of superheat, the analysis predicts the amplitude of the acoustic pressure may be on the order of an atmosphere. The initial increase in liquid pressure due to channel confinement feeds back and reduces the bubble growth rate. Because growth diminishes with cross-sectional area, less heat is transferred as d_h decreases, provided all other conditions are identical. Consequently, microchannels do not improve the heat transfer for single bubbles during the early stages of nucleate boiling. The equations describing the generation of these acoustic pressures lead to a nondimensional number, $\mathrm{Co}_{\mathrm{FG}}$, capable of predicting when bubble growth and heat transfer will be significantly inhibited in microchannels.

The limited capacity to accommodate the mass displaced during the growth of a single bubble can lead to large pressure perturbations to the steady-state flow profile. The initial pressure waves inhibit further nucleation and growth and may deactivate potential nucleation sites, while the reflected waves decrease the local pressure to levels that can allow nucleation in regions incompressible analysis does not predict.

The design of a microchannel heat exchanger, including all components up to the inlet and outlet tubing, significantly influences the nucleation characteristics in the channels themselves. Sites that would not normally generate bubbles can become active due to the pressure depressions created by the reflected acoustic pressures. As a result, the boiling heat transfer characteristics of microchannel systems are tied to the system design. Although the error due to water hammer effects may fall within the experimental error of the measurements, the influence of liquid compressibility on metrics such as heat transfer rate and mass quality have yet to be quantified. Studies of identical microchannels and channel arrays may have vastly different heat transfer results due to differences in the manifold and tubing designs making it extremely difficult to compare the different data sets. Even different chips from the same processing batch might have large differences in performance due to the random distribution of potential nucleation sites within the channels.

The bubble-induced water hammer provides an additional design factor previous unidentified. Its impact is amplified with increasing thermal loads or diminishing channel dimensions. Increases in flow instability directly compete against the additional evaporation and associated heat transfer. Whether future channels will be manufactured to amplify or dissipate these pressure pulses depends on the net benefit imposed by these opposing effects.

Acknowledgment

Dr. Fogg was supported by the Naval Nuclear Propulsion Fellowship Program sponsored by Naval Reactors Division of the U.S. Department of Energy. The authors acknowledge the support of the Interconnect Focus Center, one of five research centers funded under the Focus Center Research Program, a Semiconductor Research Corporation program, and appreciate support from the Semiconductor Research Corporation through Task 1445.

Nomenclature

a = sound speed (m)
Co = confinement number
Cp = specific heat (J/kg K)
C_{con} = confinement threshold
d_h = hydraulic diameter (m)
$\mathcal{F}$ = force (N)
$\mathcal{G}$ = geometry factor (m)
h = heat transfer coefficient (W/m K)
H = height (m)
i = enthalpy (J/kg)
L = length (m)
m = mass (kg)
nb = number of bubbles
P = pressure (Pa)
P_h = heated perimeter (m)
q = heat transfer (J)
r = radius (m)
R = specific gas constant (J/kg K)
T = time (s)
T = temperature (K)
U = axial velocity (m/s)
V = volume (m^3)
W = width (m)
z = axial coordinate (m)
α = void fraction
δ_{th} = thermal boundary layer thickness (m)
Λ = thermal diffusivity (m^2/s)
η = kinematic viscosity (m^2/s)
ρ = density (kg/m^3)
σ = surface tension (N/m)
υ = specific volume (m^3/kg)

Subscripts

0 = reference value
b = bubble
boil = boiling at standard temperature and pressure
b,s = bubble surface
c = critical property
ch = channel
con = confinement
FG = Fogg–Goodson
KC = Kew–Cornwell
l = liquid
lv = liquid-to-vapor
meas = measured
ns = nucleation site
pred = predicted
RP = Rayleigh–Plesset
sat = saturation
sup = superheat
tp = two-phase
v = vapor
w = wall

References

[1] Prasher, R. S., Chang, J. Y., Sauciuc, I., Narasimhan, S., Chau, D., Chrysler, G., Myers, A., Prstic, S., and Hu, C., 2005, "Electronic Package Technology Development," Intel Technol. J., **9**(4), pp. 285–296.
[2] Zhang, L., Koo, J.-M., Jiang, L., Goodson, K. E., Santiago, J. G., and Kenny, T. W., 2001, "Study of Boiling Regimes and Transient Signal Measurements in Microchannels," 11th International Conference on Solid-State Sensors and Actuators, Munich, Germany, pp. 1514–1517.
[3] Qu, W. A., and Mudawar, I., 2002, "Transport Phenomena in Two-Phase Micro-Channel Heat Sinks," ASME Paper No. IMECE2002-33711.
[4] Peles, Y., 2003, "Two-Phase Boiling Flow in Microchannels—Instabilities Issues and Flow Regime Mapping," ASME Paper No. ICMM2003-1069.
[5] Boure, J. A., Bergles, A. E., and Tong, L. S., 1973, "Review of Two-Phase Instability," Nucl. Eng. Des., **25**, pp. 165–192.
[6] Carey, V., 1992, *Liquid-Vapor Phase-Change Phenomena*, Taylor & Francis, London.
[7] Balasubramanian, P., and Kandlikar, S. G., 2003, "High Speed Photographic Observation of Flow Patterns During Flow Boiling in Single Rectangular Minichannel," ASME Paper No. HT2003-47175.
[8] Hetsroni, G., Klein, D., Mosyak, A., Segal, Z., and Pogrebnyak, E., 2003, "Convective Boiling in Parallel Micro-Channels," ASME Paper No. ICMM2003-1007.
[9] Jiang, L., Wong, M., and Zohar, Y., 2001, "Forced Convection Boiling in a Microchannel Heat Sink," J. Microelectromech. Syst., **10**(1), pp. 80–87.
[10] Zhang, L., Koo, J. M., Jiang, L., Asheghi, M., Goodson, K. E., Santiago, J. G., and Kenny, T. W., 2002, "Measurements and Modeling of Two-Phase Flow in Microchannels With Nearly-Constant Heat Flux Boundary Conditions," J. Microelectromech. Syst., **11**, pp. 12–19.

[11] Lee, M., Wong, M., and Zohar, Y., 2003, "Integrated Micro-Heat-Pipe Fabrication Technology," J. Microelectromech. Syst., **12**(2), pp. 138–146.
[12] Fogg, D., Flynn, R., Hidrovo, C., Zhang, L., and Goodson, K., 2004, "Fluorescent Imaging of Void Fraction in Two-Phase Microchannels," Pisa, Italy, Paper No. SGK07.
[13] Chavan, N., Bhattacharya, A., and Iyer, K., 2005, "Modeling of Two-Phase Flow Instabilities in Microchannels," Paper No. ICMM2005-75048.
[14] Koo, J. M., Im, S., Jiang, L., and Goodson, K. E., 2005, "Integrated Microchannel Cooling for Three-Dimensional Electronic Architectures," ASME J. Heat Transfer, **127**, pp. 49–58.
[15] Ajaev, V. S., and Homsy, G. M., 2003, "Mathematical Modeling of Constrained Vapor Bubbles," ASME Paper No. ICMM2003-1072.
[16] Mukherjee, A., and Kandlikar, S. G., 2004, "Numerical Study of the Growth of a Vapor Bubble During Flow Boiling of Water in Microchannels," ASME Paper No. ICMM2004-2382.
[17] Mukherjee, A., and Kandlikar, S. G., 2005, "Numerical Study of the Effect of Inlet Constriction on Bubble Growth During Flow Boiling in Microchannels," ASME Paper No. ICMM2005-75143.
[18] Zhang, J. T., Peng, X. F., and Peterson, G. P., 2000, "Analysis of Phase Change Mechanisms in Microchannels Using Cluster Nucleation Theory," Microscale Thermophys. Eng., **4**(3), pp. 177–187.
[19] Inasaka, F., Adachi, M., Shiozaki, K., Aya, I., and Nariai, H., 2005, "Water Hammer Caused by Rapid Gas Production in Severe Accident in a Light Water Reactor," JSME Int. J., Ser. B, **48**(1), pp. 48–55.
[20] Brennen, C. E., 1995, *Cavitation and Bubble Dynamics*, Oxford University Press, New York.
[21] Lu, X., Properetti, A., Toegel, R., and Lohse, D., 2003, "Harmonic Enhancement of Single-Bubble Luminescence," Phys. Rev. E, **67**, p. 056310.
[22] Plesset, M. S., and Zwick, S. A., 1952, "A Nonsteady Heat Diffusion Problem With Spherical Symmetry," J. Appl. Phys., **23**(1), pp. 95–98.
[23] Lee, J., and Mudawar, I., 2005, "Two-Phase Flow in High-Heat-Flux Micro-Channel Heat Sink for Refrigeration Cooling Applications: Part II—Heat Transfer Characteristics," Int. J. Heat Mass Transfer, **48**, pp. 941–955.
[24] Qu, W., and Mudawar, I., 2003, "Flow Boiling Heat Transfer in Two-Phase Micro-Channel Heat Sinks—I Experimental Investigation and Assessment of Correlation Methods," Int. J. Heat Mass Transfer, **46**, pp. 2755–2771.
[25] Wark, K., 1995, *Advanced Thermodynamics for Engineers*, McGraw-Hill, New York.
[26] Ferziger, J. H., and Peric, M., 2002, *Computational Methods for Fluid Dynamics*, Springer-Verlag, New York.
[27] Fogg, D., and Goodson, K. E., 2006, "The Effects of Liquid Compressibility on the Nucleation and Growth of Bubbles in Forced Convective Flow Boiling Within Microchannels," ASME Paper No. ICNMM2006-96208.
[28] Sabersky, R., Acosta, A. J., Hauptmann, E. G., and Gates, E. M., 1999, *Fluid Flow*, Prentice-Hall, Upper Saddle River, NJ.
[29] Ghidaoui, M. S., Zhao, M., Mcinnis, D. A., and Axworthy, D. H., 2005, "A Review of Water Hammer Theory and Practice," Appl. Mech. Rev., **58**, pp. 49–76.
[30] Lee, M., Cheung, L. S. L., Lee, Y. K., and Zohar, Y., 2005, "Height Effect on Nucleation-Site Activity and Size-Dependent Bubble Dynamics in Microchannel Convective Boiling," J. Micromech. Microeng., **15**, pp. 2121–2129.
[31] Hetsroni, G., Klein, D., Mosyak, A., Segal, Z., and Pogrebnyak, E., 2003, "Convective Boiling in Parallel Micro-Channels," Microscale Thermophys. Eng., **8**, pp. 403–421.
[32] Kandlikar, S. G., 2004, "Heat Transfer Mechanisms During Flow Boiling in Microchannels," ASME J. Heat Transfer, **126**, pp. 8–16.
[33] Kandlikar, S. G., 1990, "A General Correlation for Saturated Two-Phase Flow Boiling Heat Transfer Inside Horizontal and Vertical Tubes," ASME J. Heat Transfer, **112**, pp. 219–228.
[34] Kramer, T., Flynn, R. D., Fogg, D. W., Wang, E. N., Hidrovo, C. H., Goodson, K. E., Prasher, R. S., Chau, D. S., and Narasimhan, S., 2004, "Microchannel Experimental Structure for Measuring Temperature Fields During Convective Boiling," ASME Paper No. IMECE2004-61936.
[35] Bergant, A., Simpson, A. R., and Tijsseling, A. S., 2006, "Water Hammer With Column Separation: A Historical Review," J. Fluids Struct., **22**(2), pp. 135–171.
[36] Lam, K. W., Drake, J. M., and Cobbold, R. S. C., 1999, "Generation and Maintenance of Bubbles in Small Tubes by Low-Frequency Ultrasound," J. Acoust. Soc. Am., **106**(6), pp. 3719–3729.
[37] Kandlikar, S. G., and Grande, W. J., 2002, "Evolution of Microchannel Flow Passages-Thermohydraulic Performance and Fabrication Technology," Heat Transfer Eng., **25**(1), pp. 3–17.
[38] Mehendale, S. S., Jacobi, A. M., and Shah, R. K., 2000, "Fluid Flow and Heat Transfer at Micro- and Meso-Scales With Application to Heat Exchanger Design," Appl. Mech. Rev., **53**(7), pp. 175–193.
[39] Kew, P., and Cornwell, K., 1997, "Correlations for Predictions of Boiling Heat Transfer in Small Diameter Channels," Appl. Therm. Eng., **17**, pp. 705–715.
[40] Balasubramanian, P., and Kandlikar, S. G., 2005, "Experimental Study of Flow Patterns Pressure Drop, and Flow Instabilities in Parallel Rectangular Minichannels," Heat Transfer Eng., **26**(3), pp. 20–27.
[41] Li, H. Y., Lee, P. C., Tseng, F. G., and Pan, C., 2004, "Two-Phase Flow Phenomena for Boiling in Two Parallel Microchannels," ASME Paper No. ICMM2004-2384.